Organ- and function-specific anatomical organization and bioelectronic modulation of the vagus nerve

Naveen Jayaprakash[1], Viktor Toth[§1], Weiguo Song[§1], Avantika Vardhan[1], Todd Levy[1], Jacquelyn Tomaio[2], Khaled Qanud[1], Ibrahim Mughrabi[1], Yao-Chuan Chang[1], Moontahinaz Rob[3], Anna Daytz[4], Adam Abbas[5], Jason Ashville[6], Anna Vikatos[7], Umair Ahmed[1], Zeinab Nassrallah[4], Bruce Volpe[1], Kevin J. Tracey[1], Yousef Al-Abed[1], Timir Datta-Chaudhuri[1], Larry Miller[1], Mary Barbe[8], Sunhee Lee[1], Theodoros Zanos[1], Stavros Zanos*[1]

[1] Feinstein Institutes for Medical research, Manhasset, New York. [2] The City University of New York, New York. [3] Northwell Health, New York .[4] Donald and Barbara Zucker School of Medicine at Hofstra/Northwell, Hempstead, New York. [5] University at Buffalo Jacobs School of Medicine and Biological Sciences, Buffalo, New York. [6] NYIT College of Osteopathic Medicine, Glen Head, New York. [7] The Bronx High School of Science, Bronx, NY. [8] Temple University, Philadelphia, Pennsylvania.

*Corresponding author. Email: szanos@northwell.edu

([§]) These 2 authors contributed equally to this work.

Abstract

Afferent and efferent fibers in the vagus travel inside nerve fascicles and form branches to innervate organs and regulate organ functions. The organization of fibers and fascicles in the vagus trunk, with respect to the functions they mediate and the organs they innervate, remains largely unknown. Accordingly, it is unknown whether that anatomical organization can be leveraged by bioelectronic devices for function- and organ-specific neuromodulation. To characterize the microscopic functional anatomy of the vagus we developed a pipeline consisting of micro-computed tomography-based morphometry of fascicles and quantitative immunohistochemistry of single fibers. We found that, in the swine vagus, fascicles form clusters specific to afferent and efferent functions, increasingly separated in the rostral direction, and other clusters specific to the innervated organs, including larynx, lungs and heart, increasingly separated in the caudal direction. Large myelinated and small unmyelinated efferents have small counts, occupy large area of the nerve, and are limited to specific fascicles; small unmyelinated afferents have large counts, occupy small area, and are uniformly distributed across fascicles. To test whether fiber populations can be selectively modulated, we developed a multi-contact cuff electrode that observes the fascicular vagus anatomy. Targeting of different nerve sub-sections evokes compound action potentials from different fiber types and elicits differential organ responses, including laryngeal muscle contraction, cough reflex, and changes in breathing and heart rate. Our results indicate that vagus fibers are spatially clustered according to functions they mediate and organs they innervate and can be differentially modulated by spatially selective nerve stimulation.

Introduction

The autonomic nervous system maintains physiological homeostasis in organs and systems through an interconnected network of neural reflexes. Autonomic reflexes are comprised of sensory neurons that detect changes in physiological parameters, and motor neurons that modulate organ functions in response to sensed physiologic changes. With its large number of afferent (sensory) and efferent (motor) fibers, the vagus is the main conduit of bidirectional communication between the brain and body organs and a component of autonomic reflexes regulating the function of the cardiovascular and respiratory system, among others. In the human vagus, nerve fibers are arranged in fascicles, longitudinal bundles within the nerve separated by connective tissue [1, 2] [3]. Along the cervical and thoracic vagus, afferent and efferent fibers leave the fascicles and emerge to form nerve branches, which in turn provide sensory and motor innervation to the heart, the airways and the lungs [4, 5]. Even though much is known about the macroscopic and microscopic anatomy of the vagus, the spatial organization of fascicles and fibers within the nerve, as it relates to the innervated organs and the sensory and motor functions of the vagus, remains unknown.

The spatial organization of fibers in the human vagus has implications for bioelectronic therapies of diseases in which autonomic reflexes are implicated, including heart failure [7], inflammatory bowel disease [8] and rheumatoid arthritis [8]. Bioelectronic therapies use implanted electrode devices that stimulate the vagus aiming to alter the activity of vagus fibers and modulate autonomic functions in specific organs. However, current devices deliver electrical energy all around the vagus, without considering how fibers are organized in the nerve, sometimes resulting in clinically significant side effects [1, 10-13]. The anatomical organization of the vagus could be leveraged by appropriately designed electrodes that target specific sub-populations of fibers in the nerve. More selective devices could lead to reduced side-effects [11, 14], expand the indications of bioelectronic therapies to organs that are currently not targeted [15, 16], and allow the mechanistic study of specific components of autonomic reflexes in health and disease.

In this study, we developed a quantitative anatomical pipeline to characterize the organization of the vagus nerve, at the level of functional fiber types, fascicles and organ branches, in the swine, the preferred animal model for the human vagus [1, 3]. We discovered rich anatomical organization of fibers within the vagus, with fascicles and fibers clustered in separate groups with regard to the specific functions they mediate and the organs they innervate. We then developed a multi-contact cuff electrode device that observes the spatial organization of fascicles in the vagus and used it to deliver spatially selective nerve stimulation. We found that by targeting different sections of the nerve we are able to evoke action potentials from different functional types of nerve fibers and elicit differential responses from organs innervated by the vagus.

Results

Fascicles form organ-specific clusters along the vagus

The vagus in swine is highly fascicular, with 40-50 fascicles of varying sizes in the cervical region [Suppl. Figure S1]. Branches derived from the cervical and thoracic vagus provide sensory and motor innervation to visceral organs [5], including the larynx and pharynx, through the superior and recurrent laryngeal nerves [16], the heart, through the cardiac branch [5, 18], and the lower airways and lungs, through the bronchopulmonary branches [19]. To understand the spatial arrangement of fascicles with respect to the formation of vagus branches, we performed high resolution micro-computed tomography (μCT) imaging of the vagus nerve trunk, from the nodose ganglion, rostrally, to the lower thoracic portion of the nerve, caudally. Fascicles with any visible contribution to the formation of a vagus branches were manually annotated at individual sections taken through the branching point (Suppl. Figures S2, S3, S4) and were considered to project to the corresponding organ (Figure 1A). The longitudinal trajectories of those fascicles were then tracked in all μCT images along the length of the vagus rostrally with the use of an automated image segmentation algorithm. The longitudinal trajectories of many of the fascicles in the vagus trunk were not straight but helical (Suppl. video).

We found that fascicles contributing to the bronchopulmonary (BP) branch form a cluster close to the entry level (yellow fascicles, Figure 1B, panels x and w; and Figure 1C, panels r and q); bronchopulmonary fascicles remain clustered for several centimeters rostrally (Figure 3B, panels v-s; Figure 3C, panels p-o). The recurrent laryngeal nerve (RNL) joins the trunk by contributing another cluster of fascicles (red fascicles; Figure 1B, panels r-q; Figure 1C, panels n-m). Some of those fascicles ascend in parallel to the BP cluster and some merge with it, in a “composite” BP-RLN cluster (orange fascicles; Figure 1B, panels p-o; Figure 1C, panels m-l). Both BP and RLN fascicles disappear within a few centimeters and are replaced by a cluster of combined BP-RLN fascicles which runs rostrally along the upper thoracic (Figure 1B, panel n) and the cervical vagus (Figure 1C, panel l). The cardiac branch joins the vagus trunk rostrally to the RLN entry and forms a separate cluster of fascicles (blue fascicles; Figure 1B, panel o; Figure 1C, panel l). Some of the cardiac fascicles maintain their separate trajectories all the way through the upper thoracic and cervical vagus (Figure 1B, panels l-d; Figure 1C; panels k-d) and some merge with the composite BP-RLN fascicles to form a larger composite cluster of BP-RLN-cardiac (green fascicles; Figure 1B, panels m and above; Figure 1C, panels e and above). Many of the combined BP-RLN-cardiac fascicles terminate in the nodose ganglion, and some of them bypass it (Figure 1B, panels b, a; Figure 1C, panels b, a). Fascicular branching, where one fascicle branches to from two fascicles, or fascicular merging, where two fascicles merged to form one fascicle is observed throughout the length of the nerve (Suppl. Figure S5, and Supplementary video 1). These findings indicate that fascicles in the thoracic and cervical vagus trunk form spatially distinct organ-specific clusters close to the levels of entry of branches to those organs; clusters progressively merge into larger composite clusters in the caudal to rostral direction.

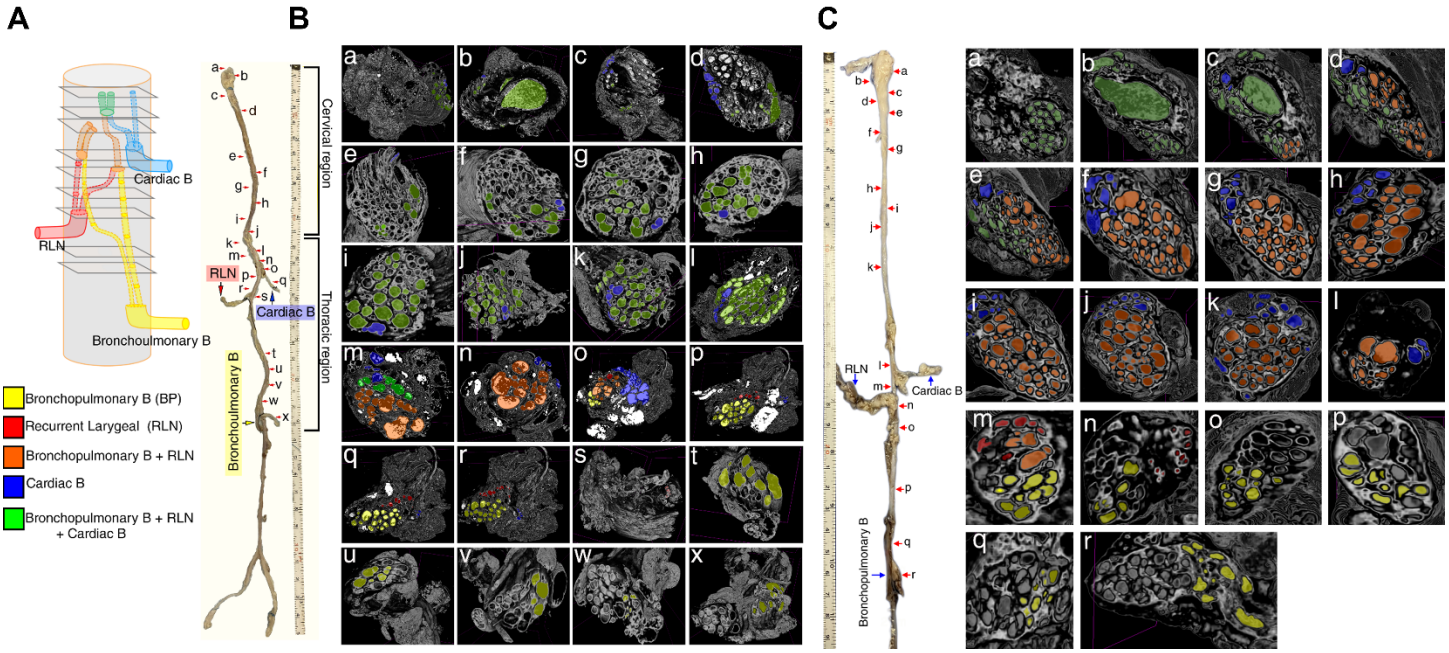

Figure 1. Fascicles form organ-specific clusters along the vagus. (A) Schematic showing a segment of the vagus trunk with 3 branches joining it (bottom to top): bronchopulmonary (BP, yellow), recurrent laryngeal nerve (RLN, red), cardiac branch (blue). The trajectories of fascicles contributing to each branch were traced rostrally inside the trunk, even after they merged with other fascicles to form "combined" fascicles: BP and RLN (orange), BP, RLN and cardiac (green). (B) Macroscopic structure of an intact right vagus trunk, from the nodose ganglion to the lower thoracic level (left). On the right, multiple micro-computed tomography sections through the trunk are shown (panels a-x), with fascicles contributing to each of the identified branches or combinations of branches shaded in the corresponding colors. (C) Macroscopic and fascicular structure of an intact left vagus trunk from a second animal.

Fascicles form separate afferent and efferent clusters along the vagus

To understand the spatial arrangement of fascicles with respect to the afferent or efferent function, we analyzed the μCT images in the opposite direction, from rostral to caudal: fascicles that terminate in the nodose ganglion were considered (primarily) afferent and those that bypass the nodose ganglion were considered (primarily) efferent (Figure 2A, panels a, b). By tracking those fascicles caudally, we found that afferent and efferent fascicles form separate clusters throughout the cervical vagus (Figure 2A, panels a to i). To examine whether the separation of afferent and efferent fascicles persists at the single fiber level, we performed immunohistochemistry (IHC) in sections through the nodose ganglion, mid-cervical and thoracic region (Figure 2B, Suppl. Figure S6 and S7).

At the nodose ganglion level (Figure 2B, panel a), ChAT-positive (ChAT+) fibers, indicative of efferent function, were almost absent (Figure 2B, panel b) but were frequently observed in fascicles outside of the nodose ganglion (Figure 2B, panel c). On the other hand, Nav1.8-positive (Nav1.8+) sensory neurons are found in the nodose ganglion as pseudo-unipolar cells (Figure 2B, panel d; and Suppl. Figure S8); smaller numbers of Nav1.8+ clusters were observed in fascicles outside of the nodose ganglion (Figure 2B, panel e). At the mid-cervical region (Figure 2B, panel f), separate clustering of fascicles rich in ChAT+ fibers (Figure 2B, panel g) from those poor in ChAT+ fibers was observed (Figure 2B, panel h, Suppl. Figure, S9), whereas such separation was absent in the thoracic region (Suppl. Figure, S10); Nav1.8+ fibers were seen in both fascicle clusters (Figure 2B, panel i & j). These findings indicate that primarily afferent and primarily efferent fascicles form spatially distinct clusters in the upper and mid-cervical trunk of the vagus; the clusters become progressively less separated moving from the rostral to caudal directions, and in the thoracic region the afferent-efferent separation no longer exists.

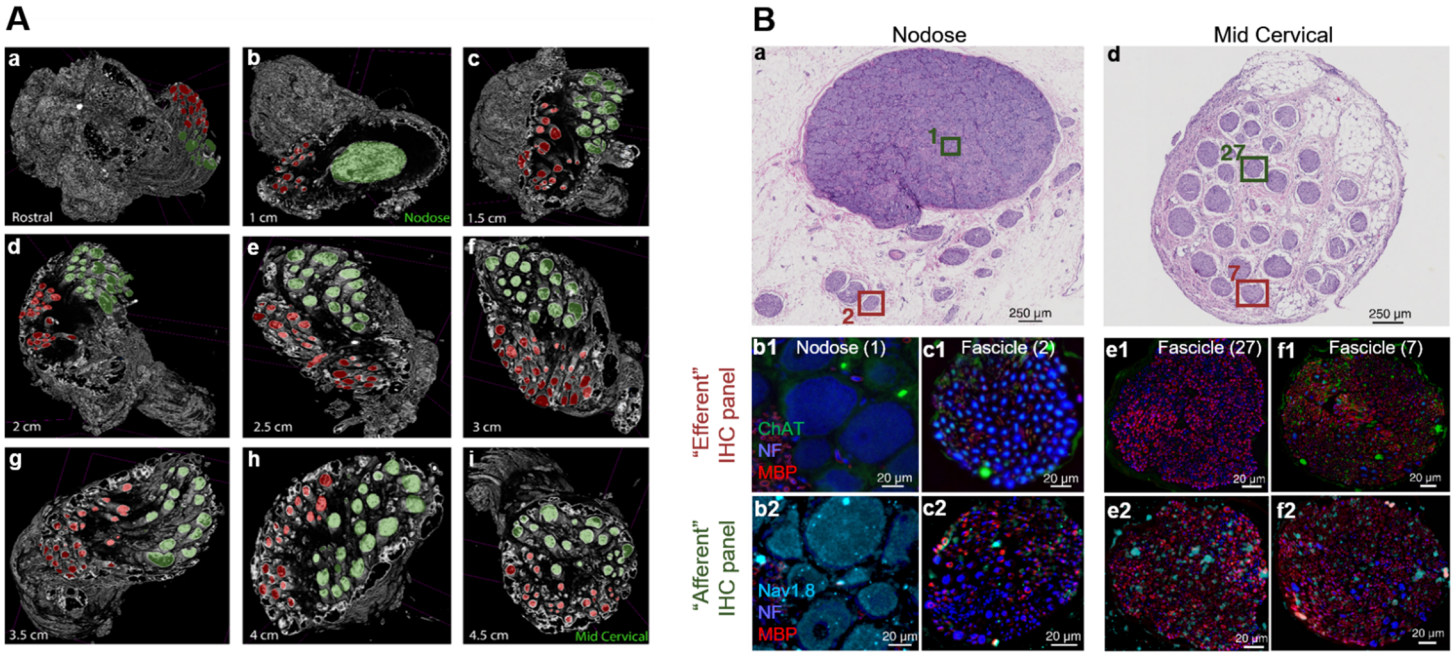

Figure 2. Afferent and efferent fascicles form clusters along the vagus. (A) Micro-computed tomography imaging of the cervical region of an intact right vagus trunk, from the nodose ganglion to the mid-cervical level. Fascicles that originate in the nodose ganglion were considered primarily afferent (shaded green), and those that "by-passed" the nodose were considered primarily efferent (shaded red). Panels (a-i) show the trajectories of afferent and efferent fascicles in consecutive sections through the cervical vagus, at different levels (shown in cm from the rostral end of the sample). (B) Imaging of afferent and efferent fibers in primarily afferent and primarily efferent fascicles. (a) H&E section at the level of the nodose ganglion. An area inside the ganglion (1) and a primarily efferent fascicle (2) are selected. (b1) Nodose area stained with an "efferent" panel of antibodies for immunohistochemistry (IHC), consisting of anti-neurofilament antibody (NF, blue) that labels nerve fibers, anti-myelin basic protein antibody (MBP, red) that labels myelin, and choline-acetyl-transferase (ChAT, green) that labels efferent, cholinergic, fibers. (b2) The same nodose area stained with an "afferent" IHC panel, consisting of NF, MBP and anti-Nav1.8 antibody (cyan) that labels afferent fibers. (c1) Fascicle (2) stained with an efferent IHC panel. (c2) Fascicle (2) stained with an afferent IHC panel. (d) H&E section at the mid-cervical level. A primarily afferent (27) and a primarily efferent fascicle (7) are selected. The 2 fascicles are stained with an efferent (e1 and f1, respectively) and an afferent IHC panel (e2 and f2, respectively).

Functional types of nerve fibers are specifically organized across and within fascicles in the cervical vagus

The human and swine vagus contain fibers of several types, including myelinated and unmyelinated afferents and efferents [2, 11, 12]. Large myelinated efferents (Aα-type) provide somatic innervation to laryngeal muscles [19, 20]; smaller myelinated efferents (B-type) are typically cholinergic and provide parasympathetic innervation to visceral organs, like the heart and the GI tract [20]. Large myelinated afferents (Aβ -type) provide sensation to the pharyngeal and laryngeal mucosa [21-23], ([24-26]) whereas smaller ones (Aδ-type) project to mechanical and chemical sensory receptors in visceral organs [27-30], ([31-34]. Finally, unmyelinated (C-type) efferents are primarily sympathetic fibers to visceral organs [35-37] ([23, 30, 35], whereas C-type afferents provide nociception, mechanical and chemical sensation to visceral organs [22, 28, 29, 38] ([25, 32, 33, 39]. To understand the spatial organization of vagus fibers in the cervical region, the most common anatomical location for stimulation electrodes, we developed a quantitative IHC pipeline, consisting of IHC staining, imaging and automated fiber segmentation, feature extraction and analysis of fibers. Based on the expression pattern of fiber-specific IHC markers, we classified each fiber as myelinated efferent (MEff, Figure 3A,a), myelinated afferent (MAff, Figure 3A, b), unmyelinated efferent (UEff, Figure 3A, c) or unmyelinated afferent

(UAff, Figure 3A, d). For UAff fibers in particular, that do not stain for neurofilament (NF), we considered individual Nav1.8+ fibers clustered in Remak bundles [40, 41], surrounded by the cytoplasm of non-myelinating S100+ Schwann cells (Figure 3B; Suppl. figure S11).

	A	B	C	D	E	F	G	H	I				
	Fiber type	Erlanger Gasser class.	Side	% Fiber area in nerve, mean [range]	Fiber count in nerve, mean [range]	% Fiber count in nerve, mean [range]	% Fiber area in fascicle, mean [range]	Fiber count in fascicle, mean [range]	Fiber type features				
									NF	MBP	ChAT	Nav1.8	Diameter (µm), mean (IQR)
1	Myel. eff. (MEff)	Aα, Aγ & B	L R	33 [28–35] 31 [15–43]	14.8K [12.7–16.6] 14.6K [4.9–21.4]	4.2 [2.7–6.4] 5.1 [0.7–8.7]	29 [0–83] 29 [0–83]	335 [0–2,419] 403 [0–1,879]	+	+	+	NA	3.47 (1.46)
2	>10 µm	Aα	L R	1.9 [0.4–4.6] 1.8 [0.5–4.5]	52 [12–130] 54 [12–127]	0.01 [0–0.03] 0.01 [0–0.02]	1.25 [0–27] 1.20 [0–19]	1.2 [0–33] 1.5 [0–21]	+	+	+	NA	15.7 (5.93)
3	<3 µm	B	L R	15 [12–20] 16 [4–27]	11.6K [9.5–13.5] 11.8K [3.4–18.7]	3.3 [2.0–5.2] 4.2 [0.5–7.6]	13.8 [0–48] 14.5 [0–57]	14 [0–48] 32 [0–57]	+	+	+	NA	3.06 (1.05)
4	Myel. aff. (MAff)	Aβ & Aδ	L R	52 [50–56] 58 [48–74]	34.0K [29.7–37.6] 28.7K [25.8–31.4]	9.1 [7.8–11.2] 8.7 [5.2–10.5]	54 [0–86] 59 [12–92]	766 [0–2,753] 790 [20–3,401]	+	+	–	NA	3.10 (1.42)
5	>5 µm	Aβ	L R	3.6 [1.2–5.7] 14 [1.7–36]	409 [163–623] 1,348 [178–3,109]	0.10 [0.06–0.14] 0.30 [0.02–0.59]	3.1 [0–20] 10 [0–54]	9 [0–56] 37 [0–510]	+	+	–	NA	8.49 (2.98)
6	2-5 µm	Aδ	L R	40 [37–42] 37 [33–42]	20.4K [17.7–22.4] 17.6K [13.9–21.2]	5.5 [4.7–6.8] 5.3 [3.2–7.1]	41 [0–72] 40 [0–83]	41 [0–72] 48 [0–84]	+	+	–	NA	3.72 (1.21)
7	Unmyel. eff. (UEff)	C-Symp.	L R	6.9 [5.1–8.8] 4.7 [2.9–7.4]	21.8K [15.1–25.7] 15.8K [10.8–23,3]	6.3 [3.1–9.8] 4.9 [2.4–7.8]	8.9 [0.6–54] 6.6 [0.7–35]	492 [9–3,084] 434 [26–1,626]	+	–	–	NA	1.83 (0.78)
8	Unmyel. aff. (UAff)	C-Aff.	L R	7.6 [5.1–10.2] 6.3 [5.1–7.9]	315K [190.0–414.0] 294K [186.0–470.0]	80 [72–86] 81 [75–91]	7.2 [1–28] 5.3 [1–16]	7.0K [2.0–63.0] 8.0K [2.0–78.0]	–	–	NA	+	0.55 (0.32)

Table I. Fiber counts and associated areas of coverage (relative and absolute) of different fiber types in the cervical vagus. Different fiber types (rows 1-8) according to criteria used in our pipeline (A) and corresponding fiber types according to Erlanger-Gasser classification (B). (C) Nerve side (left or right). (D) Percentage of fiber-covered area in the entire nerve corresponding to a given fiber type; shown is mean and range across 8 nerves. (E) Absolute fiber count of given fiber type in the entire nerve. (F) Percentage of given fiber type among all fibers in the whole nerve. (G) Percentage of area covered by given fiber type in single fascicles; mean [range] across all fascicles, of all nerves. (H) Absolute count of given fiber type in single fascicles. (I) Fiber type-specific features used in our pipeline to classify single fibers: positive (+) or negative (-) in NF stain, MBP (myelin basic protein) stain, ChAT (choline-acetyl-transferase) stain, and Nav1.8 stain. Measured diameters for each fiber type (in µm, mean and interquartile range).

Overall, we counted 200-450K individual fibers in each nerve, with more than 80% of them of the UAff type; however, UAff fibers take up less than 10% of the total fiber-covered area in the nerve (table I). Myelinated fibers, MAff and MEff, despite representing less than 15% of total fiber count, occupy 65-85% of fiber-covered area (table I; and Suppl. Figure S12). There is substantial variability in fiber counts and in the occupied area across fascicles, for all fiber types. In both left and right cervical vagus, fascicles with large MEff fiber counts are clustered together on one side of the nerve (Figure 3C, a1 and a2), in agreement with our µCT and IHC findings (Figure 2). The few, larger Aα-type fibers were concentrated in a few fascicles within the cluster (Figure 3C, bottom left in a1 and a2), whereas the smaller, B-type fibers were more uniformly distributed within the fascicles of the cluster (Figure 3C, bottom right in a1 and a2). Fascicles with large MAff fiber counts were clustered in the opposite, side of the nerve (Figure 3C, b1 and b2). MAff fibers include intermediate size Aδ-type fibers, uniformly distributed within the cluster (Figure 3C, bottom left in b1, b2), and the fewer, larger Aβ-type fibers, concentrated in a subset of fascicles in the cluster (Figure 3C, bottom right in b1, b2). The fascicular arrangement of UEff fibers parallels that of MAff and opposes that of MEff fibers (Figure 3C, c1 and c2). Indeed, counts of UEff are negatively correlated with those of MAff fibers (Figure 3D, a) and positively correlated with those of MEff fibers (Figure 3D, b). UAff fibers are present in all fascicles, even though their fiber count varied between 50% and >80% (Figure 3C, d1 and d2). Fiber distribution fascicular maps from additional nerves are given in Suppl. Figure S13. More than 50% of all fibers in the nerve, independently of fiber type, lie within 500 µm from the epineurium (Suppl. Fig. S14 & S15), indicating that the majority of vagus

fibers can potentially be activated by epineurial cuff electrode devices. The localization of UEff fibers together with MAff fibers and away from MEff fibers is observed even at the sub-fascicular level: sectors of a fascicle with high UEff counts tend to have low MEff counts (Figure 3E, a) and high MAff counts (Figure 3E, b). Within sub-fascicular sectors, fibers of the same type tend to cluster together (main diagonal of Figure 3E, c). No spatial interaction was observed between other fiber types within the fascicle (Suppl. Figure S16). Taken together, these findings indicate that there are consistent patterns in the way fibers are organized in the cervical vagus. MAff and MEff fibers are organized in separate clusters of fascicles. UEff fibers co-localize with MAff but not with MEff fibers, in whole fascicle and in sub-fascicular sectors. UAff fibers are widely and relatively uniformly distributed across and within fascicles.

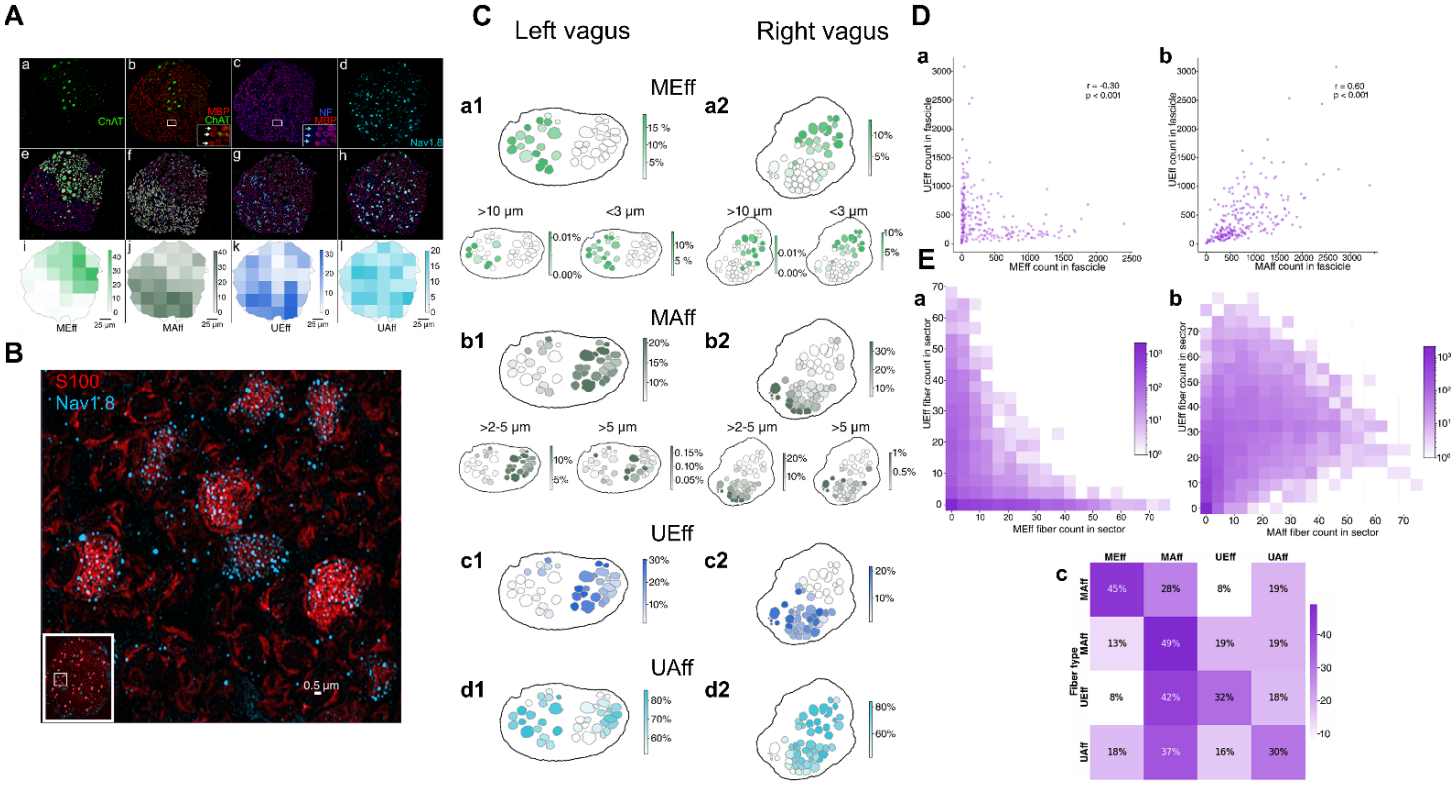

Figure 3. Functional nerve fiber types are specifically organized in the cervical vagus nerve. (A) A large-scale immunohistochemistry (IHC) and analytical pipeline was used to image, identify, characterize and classify all fibers in every fascicle. (a) ChAT+ fibers (Suppl. Figure S17) that were also NF+ and MBP+ (NF and BMP channels are not shown for clarity) were classified as myelinated efferents (MEff). (b) NF+ and MBP+ fibers that were also ChAT- were classified as myelinated afferents (MAff); white arrows point to single MAff fibers in inset. (c) NF+ and BMP- fibers were classified as unmyelinated efferents (UEff); blue arrows point to single MEff fibers in inset. (d) Nav1.8+ and MBP- fibers were classified as unmyelinated afferents (UAff). Unmyelinated afferent fibers did not stain for NF (Suppl. Fig. S18). (panels e-h) Individual fibers of each type were identified, and their features (e.g. size) and location in the fascicle were extracted. This allowed us to assess for different fiber types statistics of fiber counts, the area they cover and distributions across fascicles. (panels i-l) Local density values of each fiber type were extracted from fiber counts and locations, and projected on a fascicle using a color scale. This allowed us to assess within-fascicle arrangement of different fiber types. (B) IHC imaging of UAff fibers in a section of a nerve fascicle. Stains for Nav1.8, specific to afferent fibers, and S100, specific to non-myelinating Schwann cells, are shown superimposed to reveal several Remak bundles, within which individual UAff fibers are surrounded by the cytoplasm of Schwann cells. Inset shows the entire nerve fascicle. (C) Counts of fibers of different types in the fascicles in a section from the left and the right cervical vagus trunk of the same animal. (a1) Counts of MEff fibers across fascicles of the left vagus, as percentage of total number of fibers in each fascicle; percent counts represented by a color intensity scale. Top: Counts of all MEff fibers, independently of diameter. Bottom left: Counts of MEff fibers with diameter>10µm (Aα-type). Bottom right: Counts of MAff fibers with diameter<3µm (B-type). (a2) Same as a1, but for the right vagus. (b1) Counts of MAff fibers across fascicles of the left vagus. Top: for all MAff fibers; bottom left:

for MAff fibers with diameters 2-5μm (Aβ-type); bottom right: for MAff fibers with diameters >5μm (Aδ-type). (b2) Same as b1, but for the right vagus. (c1) Counts of UEff fibers across fascicles of the left vagus, and (c2) of the right vagus. (d1) Counts of UAff fibers across fascicles of the left vagus, and (d2) of the right vagus. (D) Distinct relationships in co-localization of different fiber types across fascicles. (a) Anti-correlated counts of MEff fibers in a fascicle (abscissa) vs. counts of UEff fibers in the same fascicle (ordinate). Each point represents a single fascicle. Shown are data from all fascicles in the cervical vagus of 4 animals (8 nerves). (b) Correlated counts of MAff and UEff fibers. (E) Distinct relationships of co-localization of different fiber types within fascicles. (a) Counts of MEff and UEff fibers within a 30-μm-square fascicular sector in all analyzed fascicles. The color intensity of each pixel represents the frequency of the specific combination of MEff-UEff fiber counts: the lighter the color, the less frequent that combination is across sectors. Shown are data from all sectors within all fascicles, from all nerves. (b) Correlated counts of MAff and UEff fibers within a 30-μm-square sector. (c) Joint probability of co-localization of different fiber types within a 30-μm-square sector. In each row, color intensity and percentage values represent the probability of finding a fiber of each of the 4 types in the immediate vicinity of the fiber type represented by that row.

Spatially selective vagus nerve stimulation differentially activates organ- and function-specific fibers

Activation or blocking of different efferent and afferent fiber populations by electric fields generated by bioelectronic devices determines end-organ effects of vagus neuromodulation therapies. Having demonstrated that vagus fibers have an organ- and function-specific organization, we next sought to test whether spatially selective VNS can differentially activate fibers innervating specific organs, as well as distinct functional fiber types. Given that intraneural electrodes may create increased risk of injury [42, 43], and that >50% of fibers lie within 500 μm from the epineurium (Suppl. Fig. S14 & S15), we developed an epineurial nerve cuff electrode. The cuff included 8 circumferentially placed contacts and 2 ring-shaped return contacts (Figure 4A). The 8-contact electrode design was chosen because, in simple computer simulations of 2-D geometric representations of vagus nerves (Suppl. Figure S19A), it attains significantly higher overall efficacy compared to designs with fewer contacts (Suppl. Figure S19B,a), with the same selectivity as other designs (Suppl. Figure S19B, b); finally it is compatible with the fascicular anatomy of the human cervical vagus (Suppl. Figure S19B, c).

Stimulation through different contacts in the multi-contact electrode produces different physiological responses from the heart, vessels, lungs and laryngeal muscles (Figure 4B). Stimulation elicits evoked compound action potentials (eCAPs), which reflect the direct activation of fibers; differential activation of fast fibers, with a conduction velocity consistent with Aα/β-type fibers; and of slow fibers, with a conduction velocity consistent with Aδ/B type-fibers, is also observed, depending on which contact is used for stimulation (Figure 4C). To characterize the physiological and fiber responses to stimulation through each of the 8 electrode contacts, threshold intensities for eliciting different organ responses were determined for each contact [43] and those thresholds were plotted on a map of the “directionality” of individual organ responses (Figure 4D). Responses from different organs have different thresholds, and those thresholds depend on which contact is used for stimulation, resulting in asymmetric directionality maps that are different for each organ response (Figure 4D). Similarly, amplitudes of fast and slow fiber activity in eCAPs depend on the stimulated contact (Figure 4E). Graded organ responses and amplitude of fibers mediating them are observed at a range of stimulus intensities, resulting in parallel recruitment curves (Figure 4F). By aligning polar plots in individual animals by the contact with the minimum heart rate threshold and normalizing responses between a minimum and maximum value, we compiled average maps of the directionality of organ responses across animals (Figure 4G). The radial location on the nerve associated with the lowest heart rate threshold on a single nerve basis (heart-specific location) was arbitrarily placed at 12 o’clock (90° angle). The vector sum of heart rate thresholds points towards the location with the greatest threshold and away from the “heart-specific” nerve location which, when averaged across 12 animals, lies at an angle of 103° (Figure 4G, a). The lung-specific nerve location lies at an angle of 128° (Figure 4G, b) and the larynx-specific location lies at an angle of 75° (Figure 4G, c). The

directionality map for blood pressure response is similar to that for heart rate response (Figure 4G,d). Similarly, by aligning polar plots in individual animals by the contact with the maximum fast fiber amplitude, arbitrarily placed at 12 o'clock (90° angle), and normalizing, we compiled average maps of the directionality of fast and slow fiber response amplitudes across animals. The fast fiber-specific location of the nerve lies at 95° (Figure 4G, a), and the slow fiber-specific location at 142° (Figure 4G, b). The larynx-specific nerve location, which was determined by measuring fast fiber-mediated laryngeal EMG responses, lies 53° clockwise to the lung-specific location, which was determined by measuring slow fiber-mediated breathing rate responses. This angular separation is similar to that between the fast fiber- and slow fiber-specific locations on the nerve, which are separated by 47° clockwise. To test whether spatial selectivity is consistent across multiple days, we performed chronic vagus implants with the multi-contact cuff electrode device in 2 animals. By stimulating through different contacts in awake sessions, we found that threshold intensities for eliciting the cough reflex, whose sensory arc is mediated by MAff fibers innervating the laryngeal and pharyngeal mucosa, are asymmetrically distributed around the nerve and, despite the gradual increase in thresholds, the overall shape of the spatial distribution is maintained for up to 3 weeks post-implantation (Suppl. Figure S20). Together, these findings indicate that the spatial organization of afferent and efferent and organ-specific fascicles and fibers in the vagus can be leveraged with a multi-contact cuff electrode to deliver spatially specific nerve stimulation, as organ and fiber responses depend on the location of the stimulated contact.

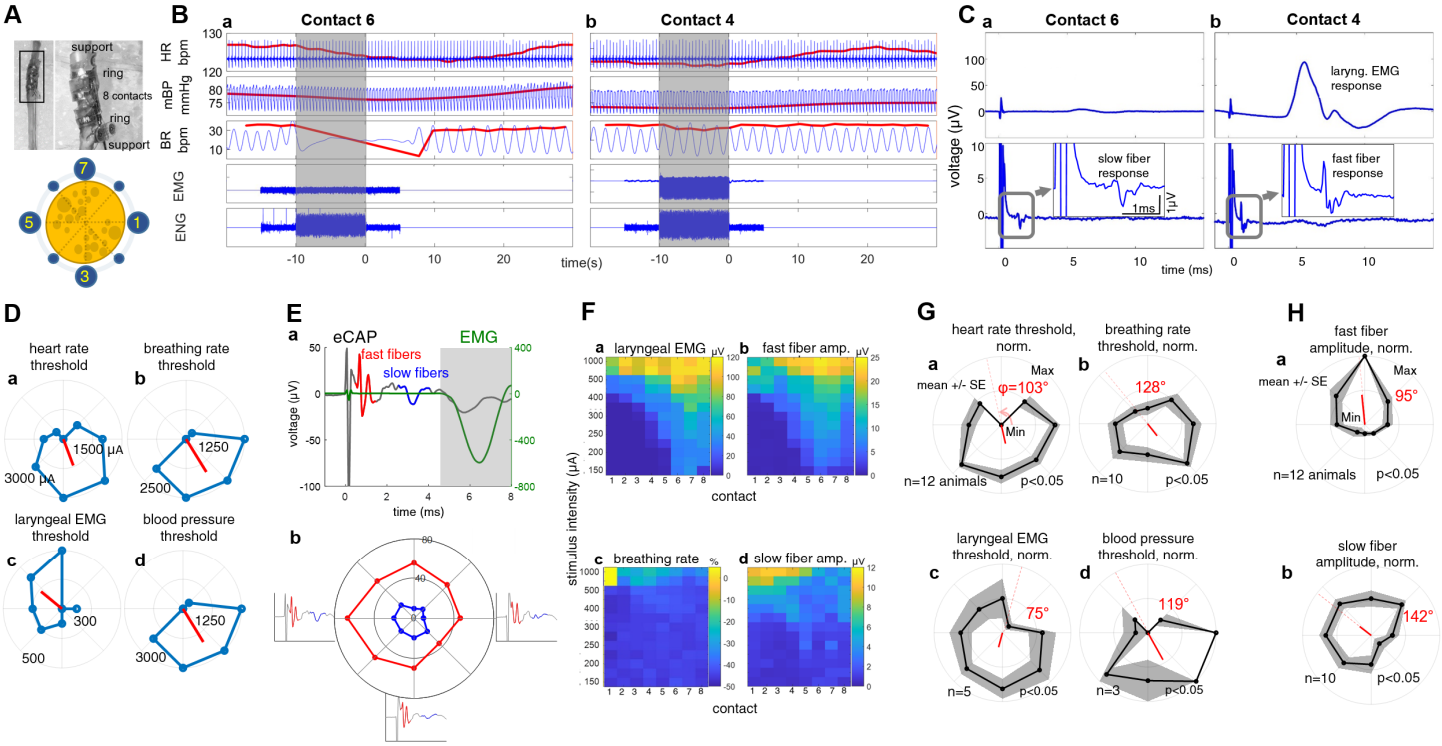

Figure 4. Spatially selective vagus nerve stimulation differentially activates organ- and function-specific fibers. (A) Helical multi-contact cuff electrode placed on the cervical vagus (left); the cuff is comprised of 2 outer support loops, 2 ring-shaped contacts, and 8 small square contacts, circumferentially placed around the nerve (right). (B) (a) Cardiovascular, respiratory and laryngeal physiological responses to a stimulus train (shaded area) through one of the 8 contacts (contact 6) include drop in heart rate (HR), a moderate drop in mean blood pressure (BP) and slowing of breathing rate (BR); at the same time, minimal evoked laryngeal muscle activity (EMG) and strong evoked responses in the nerve potential (ENG) were observed. (b) Responses to the same stimulus train delivered through a different contact (contact 4) included minimal drop in HR, BP and BR but strong laryngeal EMG. (C) (a) Evoked laryngeal EMG (top) and compound nerve action potential (eCAP, bottom) triggered by stimuli in the train delivered to contact 6. No EMG is generated and the eCAP shows a response at a latency consistent with slow A-fiber activation. (b) EMG and eCAP

triggered by stimuli delivered to contact 4; EMG response and a short latency eCAP, consistent with fast A-fiber activation, are observed. (D) Threshold intensities for different physiological responses determined for each of the 8 different contacts in the multi-contact cuff electrode: (a) threshold for HR response, (b) BR threshold, (c) laryngeal EMG threshold, (d) BP threshold. Threshold was defined as the minimum intensity of a stimulus train (200 μs pulse width, 30 Hz) that produces a change of 5-10% in the corresponding physiological variable. Shown are averages of thresholds determined from 3-5 trains in each contact, all in the same animal. (E) Fast and slow fiber responses in eCAPs elicited from each of the 8 contacts. (a) Evoked EMG activity. (b) eCAP activity with latency-based classification of fast (red trace) or slow fiber responses (blue trace). (c) Fast and slow fiber amplitudes on each of the 8 contacts. (F) Physiological responses and eCAPs mediating them have different recruitment curves from different contacts. (a) Amplitude of laryngeal EMG is shown for different stimulation contacts (abscissa) and at different intensities (ordinate), represented by the color scale (dark blue: 0μV; bright yellow: 120μV). (b) Same for amplitude of fast fiber response in the eCAP; fast fibers (e.g. Aα) mediate efferent signaling to laryngeal muscles. (c) Same for the magnitude of breathing response, quantified as % change in BR. (d) Same for amplitude of slow fiber response in the eCAP; slow fibers (e.g. Aδ) mediate afferent signaling to the brain that, through a reflex mechanism (Herring-Breuer reflex) slows down or arrests breathing. (G) Spatial distributions of normalized threshold intensities and associated “preferred directions” for physiological responses across animals. (a) Average (+/-SE) normalized HR threshold in 12 animals. The contact with minimum HR threshold in each animal is placed at 12 o’clock direction (origin of polar plot); outer circle of polar plot represents the maximum HR threshold for each animal. p value represents statistical significance of 1-way ANOVA (dependent variable: threshold, independent variable: direction of contact). Red line represents the vector sum of preferred directions of distributions from all animals; it points towards the side of the nerve with the greatest threshold (and therefore the *least* selective for the corresponding physiological response). (b) Average BR thresholds and preferred direction across 10 animals. (c) Average laryngeal EMG thresholds and preferred direction in 5 animals. (d) Average blood pressure threshold distribution in 2 animals. (H) (a) Average spatial distributions of normalized eCAP response amplitudes for fast fibers across animals. Contact with greatest fiber response amplitude is placed at 12 o’clock direction and corresponds to the outer circle; origin of the plot represents the minimum response amplitude for each animal. p value represents statistical significance of 1-way ANOVA (dependent variable: fiber response amplitude, independent variable: direction of contact). (b) Same as (a), but for slow fibers.

Discussion

In this study we demonstrate rich, functionally and translationally relevant structure in the organization of fascicles and fibers within the cervical and thoracic vagus nerve in swine. We also show that nerve stimulation in swine using a multi-contact cuff electrode device can leverage the structural organization of the vagus to differentially engage organs innervated by and physiological functions mediated by the vagus nerve. We chose the swine model because the swine vagus more closely resembles the human in its fascicular structure, effective diameter and relative thickness of the endoneurium, perineurium and epineurium, compared to rodents and non-human primates [1, 3]. On the other hand, the swine vagus has 5-10 times more fascicles than the human vagus and accordingly smaller fascicle diameters (Suppl. Figure 1), thereby representing a appropriate and challenging anatomical substrate for testing methods and technologies for selective vagus neuromodulation [2, 11, 15, 45, 46].

The vagus nerve provides several branches along its course: cervical branches, including the superior and recurrent laryngeal nerves for the larynx and pharynx [1, 47], thoracic branches, including the cardiac and bronchopulmonary nerves for the heart and the respiratory system, and numerous lower thoracic and abdominal branches, innervating the esophagus, stomach, pancreas, liver, spleen and small intestine [2]. Despite the variability in branching patterns at the nodose and cervical level [1, 47], the overall branching pattern is relatively consistent between subjects in humans and swine ([3, 48]) (Suppl. Table 1). Branches are formed by fibers that descend in the nerve trunk along fascicles, surrounded by perineurial tissue [3, 48]. By imaging fascicles contributing to individual branches with micro-CT [4] and tracking their trajectories, we discovered that organ-specific fascicles form clusters close to the levels at which branches for those organs emerge and progressively merge with clusters from other organs (Figure 1). A portion of the cardiac fascicles does not merge with other fascicles (Figure 1), a finding with potentially significant implications in the design of targeted neuromodulation therapies for cardiac diseases [49]. Recently, it was reported that vagus fascicles contributing to the formation of laryngeal nerves are grouped separately from other fascicles [1]. Our findings indicate that such separation can be explained by a more general topographic organization of fascicles, according to the organ they innervate. The presence of a “viscerotopic” organization of fibers in the trunk of the vagus is not unlike the topographic organization of motor vagal neurons in the dorsal motor nucleus of the brainstem [1] and of sensory vagal neurons in the nodose ganglion [52] and the nucleus tractus solitarius [51]. The progressive merging of fascicles from different organs suggests that, with regard to organ innervation, the cervical vagus is organized, at a large scale, in a “lattice-like” manner.

The vagus provides sensory innervation to visceral organs through afferent fibers and motor innervation through efferent fibers. By tracking trajectories of fascicles emerging from the sensory nodose ganglion (afferent fascicles) and of fascicles by-passing the nodose (efferent fascicles), we discovered a persistent spatial separation between the 2 groups of fascicles throughout the cervical vagus (Figure 2A), in agreement with the separation of efferent vagus trunk fascicles contributing to the laryngeal nerve from the remaining fascicles [1]. The afferent-efferent separation involves not only large myelinated efferents that provide somatic motor innervation to the laryngeal muscles [1], but also small myelinated efferents (Figure 3C), that provide cholinergic, parasympathetic innervation to visceral organs, and even unmyelinated efferents, that may represent adrenergic sympathetic fibers (Figure 2B; Figure 3C; Suppl. Figure S13). Large, somatosensory, and smaller, viscerosensory, myelinated afferents also observe the afferent-efferent fascicular separation (Figure 3C; Suppl. Figure S13). The afferent-efferent separation at the fascicular level may represent an organizing principle for both somatic and visceral fibers in the vagus throughout the cervical region, reminiscent of the distinct topographic arrangement of some somatic peripheral nerves [53, 54]. This finding suggests that, with regard to sensory-motor functions the cervical vagus is organized, at a large scale, in a “cable-like” manner.

A third layer of neural organization in the vagus involves several anatomically- and functionally-distinct fiber types. Large myelinated efferents (Aα-type) provide somatic innervation to laryngeal muscles [54] and smaller myelinated efferents (B-type) mediate parasympathetic regulation of visceral organs [24-26]. Large myelinated afferents (Aβ -type) provide somatic sensation to the pharyngeal and laryngeal mucosa [31-34], whereas smaller myelinated afferents (Aδ-type) project to autonomic sensory receptors in visceral organs [23, 30, 35]. Unmyelinated C-type efferents represent primarily sympathetic fibers to visceral organs [25, 32, 33, 39], whereas unmyelinated C-type afferents mediate visceral sensation [2, 12, 13]. The human and swine vagus contain fibers of all these types [48, 55]. Historically, to obtain high resolution mapping of fiber types in the vagus, electron microscopy (EM) imaging is used to visualize, classify and quantify counts of different fiber types in peripheral nerves, including the vagus [47, 58]. To discriminate between afferent and efferent fibers, selective vagotomies are performed at appropriate levels, causing selective loss of injured axons; by comparing intact and vagotomized nerves, inferences about the spatial distribution of afferent or efferent fibers can be made. In those studies, fiber quantification is done by manual annotation of EM images from randomly selected regions of the nerve; the number of fibers in the sampled area is then extrapolated to estimate the total number of fibers in the entire nerve [58]. The process is slow and cannot be used to resolve the full extent of fiber organization within and across fascicles in large nerves like the vagus in swine or humans, especially given the rich repertoire of fiber organization we describe here. While high-throughput segmentation algorithms of electron microscopy nerve images, based on U-net neural network architectures [30, 35, 56, 57], have been recently proposed, they only address the annotation part of the many bottlenecks that are involved in using EM imaging to resolve fiber organization. Moreover, even with these advanced techniques, the F1 scores of segmentation accuracy range between 0.7 to 0.9, indicating significant room for improvement.

To address these issues, we developed a quantitative anatomy pipeline for staining, imaging and automated annotation and quantification of single fibers. Antigen expressed by certain fiber types can be selectively targeted using a specific antibody tagged to a fluorophore [29, 34, 60, 61]. Since antibody binding is highly sensitive and selective only to a particular antigen, multiple antibodies with different fluorophore wavelengths can be used to identify several antigens at the same time with greater precision. For instance, in our study we used an IHC panel of antibodies against choline acetyltransferase (ChAT) (Suppl. Figure S17), neurofilament (NF) and myelin basic protein (MBP), which when they colocalize together to identify large myelinated efferent (MEff) fibers (Figure 3A). In the same panel, fibers that lack ChAT staining but are positive for NF and MBP were classified as myelinated afferents (MAff and fibers that lack ChAT and MBP are classified as unmyelinated efferents (MEff). ChAT+ fibers in previous reports were quantified using a DAB chromogen technique, at a relatively low power e.g. 20x [1, 3]. In this work, we employed immunofluorescence (IF) to detect ChAT expression. The advantage of the IF technique is the ability to colocalize the ChAT expression with NF and MBP. Also, IF enabled us to visualize individual fibers at 100x magnification, accessing the subcellular localization of the ChAT, NF, and MBP in the same axon with high selectivity and sensitivity, something not possible using the DAB chromogen technique. Small afferent fibers do not express NF (Suppl. Figure S18); therefore, they could not be identified using that marker. Using an antibody against Nav1.8, a tetrodotoxin-resistant voltage-gated channel encoded by the SCN10A gene that is expressed specifically by small afferent fibers, we were able to identify clusters of unmyelinated afferents (Figure 3B; Suppl. Figure S10; Suppl. Figure S11). Since non-myelinated Schwann cells in Remak bundles are known to encompass small unmyelinated fiber clusters, we further confirmed the accuracy of detecting C-afferent clusters by testing for co-localization with the S100 antibody expressed by the Schwann cells (Figure 3B). Using IF, we were able to identify afferent fibers that are selectively positive for Nav1.8 but negative for NF and MBP to yield annotation for UAff fibers. Measurement of the diameter of single fibers allowed us to further classify them into additional sub-types (Figure 3; table I). In our study we imaged the entire nerve and all fascicles at a resolution of 0.150 microns/pixel. At that resolution, individual axons as small as 0.3 micron diameter can be visualized and measured. The IF technique in combination with the automated algorithm to efficiently analyze very large

image sets provides unprecedented quantification of whole populations of fibers in large peripheral nerves. To the best of our knowledge, this is the first methodology that allows complete characterization of the main functional fiber types in the vagus, including small, unmyelinated fibers using light microscopy. The use of deep-learning based algorithms on anatomically guided, medical image segmentation has received Despite the increased interest in deep-learning based algorithms for anatomically guided, medical image segmentation [62], when it comes to nerve anatomical structures and segmentation, the applications of deep-learning are limited to EM [57] and ultrasound images [61]. In IHC imaging, segmentation of nerve fibers has relied on manual or semi-automated processes [62, 63]; more recently, neural networks have been used to segment and reconstruct fascicles in peripheral nerves [64]. In micro-CT and other optical tomography imaging modalities, software-aided manual segmentation is the standard in processing of fascicles and nerve structures [1, 65, 66]. However, none of these approaches takes advantage of the rich staining and imaging capabilities of IHC for characterizing fascicles and fibers. To the best of our knowledge, this is the first application of convolutional neural networks, and in particular mask-RCNN, on both micro-CT and IHC imaging data, to segment and extract anatomical features at the fascicle and single fiber level.

Using the pipeline, we were able to count, rather than estimate, all fibers in 8 vagus nerves (4 left, 4 right), at the cervical level. We also classified each of those fibers in one of 4 types: MEff, MAff, UEff and UAff (Table I; Suppl. Figure S12). Fiber type percentages we documented in the swine vagus are in agreement with those reported in the, much less fascicular, ferret [38] and cat nerves [58]: MEff ~4% of all fibers in swine (4% in ferret), MAff ~8% in swine (9% in cats and ferrets), UEff ~5% in swine (8% in ferrets, 26% in cats), and UAff >80% in swine (79% in ferrets, 54% in cats). Ours is the first quantification of the distribution of UEff fibers in the pig vagus. It is likely that many of the UEff fibers in the swine nerves are small, unmyelinated adrenergic fibers, even though we did not specifically stain for tyrosine hydroxylase (TH). In humans recent evidence suggests the presence within the vagus nerve of hitchhiking branches projecting from the cervical sympathetic chain [28]. There is possibility that a percentage of UEff fibers are non-adrenergic non-cholinergic [36]. Our study is also the first to describe the arrangement of vagal UAff fibers across entire large structures. Until now, UAff fibers have only been identified with the use of EM imaging, a process that cannot be used for large scale fiber annotation and quantification. UAff fibers comprise 60-90% of the fibers in every fascicle of the cervical vagus (Table I; Figure 3C; Suppl. Figure S13), but occupy only 5-7% of the area (Table I). This indicates that even efferent fascicles have significant numbers of UAff fibers; given that efferent fascicles bypass the nodose ganglion, it is likely that a portion of those fibers represent peripheral axons of sensory cells outside of the nodose ganglion (e.g. jugular ganglion). For all fiber types, the variation of fiber counts and occupied areas between fascicles is far greater than the variation between nerves or subjects (Table I), indicating that sampling from a subset of fascicles in a nerve may introduce estimation errors. Furthermore, fiber counts show interactions between fiber types at the fascicular and sub-fascicular level. For instance, fascicles with high UEff fiber counts tend to have low MEff fiber counts, and vice versa (Figure 3D, a); because MAff and MEff fibers are found in separate fascicles, that also means UEff and MAff fibers tend to co-localize in the same fascicles (Figure 3D, b). Similar interactions are observed at the sub-fascicular level, with certain fiber types preferring and others avoiding each other (Figure 3D, c-e). The co-localization of different combinations of afferent and efferent fiber types in the same fascicles or in the same sub-sections of fascicles suggests that the microscopic structure of the vagus may follow a “multiplexing” architecture, in which certain types of signals, from the same or different organs, are brought into close physical proximity as they are conveyed through the vagus; that organization pattern may have implications for the spatial arrangement of vagus sensory and motor neurons in the ganglia and the brainstem.

The anatomical information gained in our studies could dictate strategies for spatially selective stimulation of the vagus. Selective VNS may provide a means to tailor stimulation to the individual nerve anatomy and engage the innervation of the desired organs with fewer off-target effects [4]. The use of multi-contact

electrodes for current steering during nerve stimulation is a well-established method to deliver spatially selective stimulation, as it permits activation of sub-sets of fascicles or fibers, e.g. [69]. A similar approach has been followed in a rat model of VNS, in which reduction of blood pressure was attained without affecting heart rate and breathing rate [59]. It has also been used in a sheep model of VNS, in which fascicular stimulation attained changes in breathing rate without affecting the heart rate [16]. Because surface electrodes are less invasive than intraneural probes, and therefore carry a smaller risk of injury to the vagus, and because most vagus fibers lie within less than 500 μm from the epineurium (Suppl. Figure S14), a cuff electrode may be a viable selective interface with the vagus. In a simplified model of the spatial overlap between fascicles and contact generated electrical fields, a cuff with 8 contacts, placed on a helical substrate circumferentially around the nerve, provides close to maximal efficacy, with similar selectivity as configurations with more contacts (Suppl. Figure S19B). This configuration is compatible with the fascicular anatomy of the human vagus nerve (Suppl. S19C).

Delivering stimulation through different cuff contacts results in differential engagement of fibers innervating the larynx, the lungs and the heart, as demonstrated by the different patterns of physiological and evoked potential responses (Figure 4B). Correlations between physiological and corresponding nerve fiber responses are seen in the recruitment curves, which are also different among different contacts (Figure 4F). This indicates that the differences among contacts in the stimulation intensity thresholds arise because of differential activation of separate fiber populations. The different radial distributions of thresholds for e.g. cardiac vs. respiratory responses indicates that between-contact differences arise because of differences in the underlying fiber distribution, rather than other factors that affect one side of the nerve or the interface (e.g. thicker epineurium or looser placement of the cuff). The fact that we observe evoked compound action potentials comprised of only fast and slow A-fiber components may be related to the overrepresentation of large myelinated fibers in terms of nerve area covered (Table I) or to the stimulus intensities used in this study, that may have been below the activation thresholds for smaller fibers. Asymmetrical engagement physiological responses, related to cough reflex, was also observed in longitudinal survival experiments conducted over a period of 3 weeks after the cuff implantation, in a first report of a chronic vagus implant in swine (Suppl. Figure S20). Cough and throat pain is a common off-target effect of cervical VNS and our findings indicate that its magnitude could in principle be reduced by selective VNS. The contacts with the most cardiac selectivity (lowest heart rate threshold) on average were located (103°) in between those with the most lung selectivity (128°) and those with the most laryngeal muscle selectivity (75°) (Figure 4G). This arrangement may reflect the relative position of cardiac, bronchopulmonary and laryngeal fascicles in the trunk of the vagus (Figure 1), even though we did not co-register the exact contact locations on the specific nerve anatomy. Accordingly, the angular separation between the most fast fiber-selective contact (95°) and the most slow fiber-selective contact (142°) is in agreement with the separation between the contact with the strongest laryngeal contraction and the contact with the strongest breathing response (47° vs. 53°, respectively).

The spatial selectivity profile of a nerve interface depends on the spatial relationship between the contacts in a multi-contact cuff electrode and the underlying nerve anatomy, and will be different for every subject, even if there is an “average” overall structure across individuals. Resolving the selectivity profile on a single subject basis requires real-time or semi-real time methods. Recently, it was reported that the large-scale fascicular structure of the swine vagus can be visualized with noninvasive, high resolution ultrasound imaging [46]. Electrical impedance tomography of stimulus-elicited responses has also been used to resolve the fascicular structure of peripheral nerves [60]. In our study, we show that functional nerve mapping can be performed by quantifying physiological and/or nerve fiber responses delivered through different contacts and visualizing those on polar plots representing their spatial distribution around the nerve (Figure 4D, E). Physiological responses to short stimulus trains correlate with fiber activation by those stimulus trains (Figure 4F, and [44, 55]). Physiological responses to stimulation can be registered noninvasively in humans and experimental

animals and processed in real time, and they could be used in the bedside evaluation and calibration of selective vagus neuromodulation therapies.

Methods

Animal surgeries

The effects of VNS on physiological and neural response were examined in male pigs (Yucatan; n=13, ~50kg; Yorkshire, n=1, ~30 kg). All of the animal protocols and surgical procedures were reviewed and approved by the animal care and use committee of Feinstein Institutes for Medical Research and New York Medical College.

Anesthesia: For a 12-hour period before surgery, the animals were maintained on a no food and no fluid regimen (NPO). On the day of surgery, the animals were weighed and sedated with mixture of Ketamine (10-20 mg/kg) and Xylazine (2.2 mg/kg) or Telazol (2-4 mg/kg). Propofol (4-6 mg/kg, i.v.) was used to induce anesthesia, and following intubation, the anesthesia will be maintained with isoflurane (1.5-3%, ventilation). Mechanical ventilation will be provided and might be turned off to measure the breathing change during VN stimulation. Animals were placed on a table in a supine position with normal body temperature between maintained between 38°C and 39°C using a heated blanket and/or a hot air warmer and monitored with a rectal probe thermometer. Blood pressure and blood oxygen level were monitored with a BP cuff and a pulse oximeter sensor. The depth of anesthesia was monitored by assessing heart rate, blood pressure, respiration, and mandibular jaw tone. All surgeries were performed using sterile techniques.

For survival surgeries, a fentanyl patch (25-50 mcg/hr) and buprenorphine (0.01 mg/kg s.q.) were provided to the animal at the end of surgery to alleviate post-operative pain. After gradually weaning off the ventilator and extubated and when physiological signs returned to normal, animals were returned to the home cage and were monitored 3 times/day for 72 hours. Cefazolin (25 mg/kg p.o.) was given for 5 days. Carprofen (2-5 mg/kg, s.q.) was administered when the animal showed signs of pain. Animals were allowed 10 days for full recovery before any tests were performed.

Physiology experiments

Breathing rate: Breathing was monitored by using a respiratory belt transducer (TN1132/ST), which was placed around the belly or chest and connected to a bridge amplifier (FE221, ADI). The change of the belt pressure with breathing represented the breathing cycle and was used to derive the breathing rate. The mechanical ventilator was turned off when measuring the effects of vagus nerve stimulation on breathing.

ECG: The skin around the wrist was shaved and conductive gel was applied to patch electrodes which were subsequently adhered to the skin, ECG was recorded using a 3-lead patch electrode configuration and amplified using a commercial octal bio-amplifier (FE238, ADI).

Heart blood pressure: Ultrasonic guidance (H8018QE and Vivid iq v203 4D) was used to pass a 19 G angiographic needle through the skin at a 60-degree angle to the target vessel. Once blood backflow was detected, a soft guidewire (0.035 inches) was introduced into the vessel. A 5-Fr micro manometer-tipped catheter (SPR-751, Millar Inc) was advanced into the aorta or right ventricle, and pressure was recorded continuously after amplification (FE228 ADInstruments). The catheter locations were confirmed by verifying the characteristic phasic blood pressure waveforms corresponding to different placements.

All physiological signals were first digitized and then acquired at 1 kHz (PowerLab 16/35, ADI) and then visualized using LabChart (ADInstruments Inc).

Cervical vagus nerve implant and recording

Under the surgical level of anesthesia, a 4-5 cm long incision was cut down to the subcutaneous tissue on the right or left cervical region of the neck, 2 cm lateral to the midline. Subcutaneous tissues were dissected and retracted to expose the underlying muscle layers. The sternomastoid muscle was bluntly separated and retracted laterally away from the surgical field. The carotid sheath was exposed and the vagus nerve was identified and isolated away from the carotid artery. One or two 8-contact cuff electrodes (CorTec Inc) were placed on the rostral (around 2cm to nodose) and/or caudal sites with a distance of 4 to 5 cm after isolating the underlying 2 cm long section for each electrode. The middle portion, between the two isolated sites was left intact within the carotid bundle to minimize the extent of surgical manipulation and trauma to the nerve. For laryngeal muscle recording, after the hyoid bone was blunt dissected, Telfon-insulated single or multi-stranded stainless-steel wires were de-insulated at the tip about 1 mm, and inserted in thyroarytenoid (TA) of laryngeal muscle with a needle. For survival surgery, the incision was closed, the leads and connectors of the implanted cuff electrodes and EMG electrodes are tunneled from the surgical field in the neck area to the back of the neck subcutaneously and then to the top of the skull, where they are externalized. Several stainless-steel skull screws are implanted in the exposed area of the skull by drilling small burr holes. The connectors and the anchoring screws are secured with dental acrylic, and then a titanium casing will be attached around and secured to the skull around the connector for protection of the implants.

Neural signal and EMGs were sent to the data acquisition system through a headstage (RHS 32, Intan Tech). It was filtered (60-Hz notch), amplified, and digitized at a sampling frequency of 30 kHz with an acquisition system (Intan 128 recording/stimulating, Intan Tech).

Paradigms of vagus nerve stimulation and physiological data analysis

Physiological thresholds: Vagus nerve stimulation was found to modulate different physiological responses, and different functional fascicles were found to show topo-organizations within the nerve. Biphasic stimulus pulses were delivered through an isolated constant current stimulator (STG4008, Multichannel Systems). Physiological threshold (PT) was detected from stimulus trains of 10 s durations (30 Hz, pulse width 200 μs). There was at least 30 s long duration between successive trains to ensure that physiological measurements had reached a steady state before a new train was delivered. We define PT as the lowest stimulation intensity to induce 5% drops of HR, and 50% drop of BR as the thresholds for HR and BR, respectively. In awake animals we tested PT of cough, which is the lowest stimulation to induce coughing. The threshold of EMG was the lowest intensity to induce a visible response. The thresholds for each of the eight contacts were tested randomly.

Evoked compound action potential(eCAP): After removing the DC component (<1 Hz) from recordings, evoked compound action potentials (eCAP) from the vagus nerve were averaged across all of the individual stimulus pulses within each train. The responses (peak-to-peak) from eCAP within predefined time window were classified into different fibers based on the conduction speed. Given the distance between recording and stimulation electrode ~50 mm, the first peak latency within 1.5 ms (conduction speed, >33 m/s) was classified as a fast fiber response, and the late peak after the 2 ms was classified as slow fiber response (conduction speed, <25 m/s). In most of the recordings, EMG contamination observed in eCAP recordings could be blocked by Vecuronium. Long latency C-fiber response was not observed in our tests. The eCAP responses (peak-to-peak amplitude) from eight contacts on the second cuff were recorded simultaneously while stimulating each of the eight contacts.

Recruitment map and population responses: The responses from laryngeal muscle (peak-to-peak EMG amplitude), breathing rate change and mean eCAPs responses (8 contacts) of different fibers were characterized to inform recruitment maps during increasing stimulation intensity across 8 stimulating contacts.

To characterize the spatial selectivity of the 8-contact cuff, PTs and eCAPs from each contact were plotted on a polar-plot with mean direction and resultant vector length. To show the spatial selectivity across animals and compare difference between physiological responses, we aligned the lowest thresholds of HR on the 12 o'clock position from all animals, and then PTs of BR and EMG was aligned to the HR. Then the PTs were normalized between the lowest (to 0) and highest (to 1) to give the population (mean+/- SE) across animals. Similarly, we first aligned the highest responses (eCAP of peak-to-peak amplitude) of fast fiber to 12 o'clock position, and then we get the population eCAPs (mean+/- SE) across all animals, and finally the population response from slow fiber eCAPs were alighted to the fast response for each pig and averaged across animals (mean+/- SE). ANOVA was used to test the spatial selectivity across contacts (anova1, *$p<0.05$).

Euthanasia

At the end of the study, the swine was euthanized with a solution (Euthasol) (A dosage of 1 ml/10 pounds BW, i.v.). Euthanasia solution (Euthasol) was injected intravenously. Death was confirmed using the ECG signal and the arterial blood pressure signal. Absence of a pulse in both signals confirmed cardiac death. After euthanasia, both the left and right vagus nerve were harvested for histology.

Micro-Computed Tomography

Pigs were euthanized, and the cervical vagus nerve from both the left and right side were carefully dissected and fixed in 10% formalin for 24 hours. The nerve samples were transferred to Lugol's solution (Sigma, L6146) for five days before the micro-CT scan to achieve optimal fascicular contrast. Nerve samples were wrapped in a less dense material such as saran wrap and mounted in position on a vertical sample holder tube. The samples were scanned using Bruker micro-CT skyscan 1172 with a voxel size of 6 μm resolution. Volume rendering was done using Bruker CTvox v3.3.1 to obtain a 3D reconstructed view of the nerve (Suppl. Figure S2-S4).

Micro-Computed Tomography Tracking of Fascicles

The automated fascicle tracing approach consists of two stages: detection and tracking. We chose a mask RCNN model as our detector because it performs well on the detection task and can readily be updated in individual animals if necessary. The model was trained on 6000 (out of 7500) cross-sectional micro-CT images of a vagus nerve that were manually labeled. The tracker filters and structures the detections to construct a graph that captures properties of the fascicular cross-sections (shape and texture metrics) at each node and encodes branching and merging via the graph edges. Trackers can improve the overall performance by delaying decisions while accumulating evidence so that low-contrast fascicular segments can be discerned, and by constraining the motion of the fascicular branches as they traverse longitudinally. Individual fascicles contributing to the different vagal branches were manually identified at the branching points (Suppl. Figure S2-S4). The tracked fascicle trajectories were then color coded from the caudal end of the branching point to the rostral end of the nodose ganglion (Figure 1).

Immunohistochemistry

Cross-section of the vagus nerve at 5 μm thickness was obtained through paraffin sectioning. Sections were stained for myelin basic protein (MBP), NF, choline acetyltransferase (ChAT) and Nav1.8 using standard IHC protocol [72] to identify the number and distribution of the myelinated and non-myelinated fibers inside different fascicles. Briefly, sections were subjected to deparaffinization procedure using xylene and ethanol rinse and then washed with distilled water for 10 min. Antigen retrieval was performed by briefly subjecting the samples to 1 x citrate buffer to unmask the antigens. Sections were rinsed with 1x Tris-buffered saline and subjected to 1 hour of blocking step using one normal goat serum. Sections were incubated with anti-Neurofilament (1:500, Abcam AB8135), anti- Myelin basic protein (1:500, Abcam AB7349), anti-ChAT (Millipore Sigma, AB144P), and SCN10A Monoclonal Antibody (Nav1.8, MA5-27663 Fisher) overnight at 4 °C in a shaking humidifier. The

following day, sections were rinsed and incubated with the secondary antibody for two hours at room temperature. Slides were then rinsed thoroughly with TBS buffer three times, and cover glass was mounted on the sides with the fluoromount (Vector labs, H-1700). The slides were then imaged using ZEISS LSM 900, confocal laser scanning microscope, and BZ-X800 all-in-one fluorescence microscope at 100x magnification.

Fiber segmentation and feature extraction

We designed a set of algorithms and a data pipeline to segment and extract nerve, fascicle and single-axon level features from IHC images of the vagus. First, we developed a fiber segmentation and feature extraction algorithm by combining standard computer vision methods with statistical modeling and geometrical manipulations, including Gaussian mixture models and Voronoi tessellation, and achieved a single-axon detection accuracy of 82% and myelination classification accuracy of 89% [62]

To improve the detection accuracy, we further trained a Mask R-CNN deep convolutional neural network on axon instance segmentation. The model was pretrained on the COCO Instance Segmentation task [74]. We generated training images by first annotating fibers using the more standard algorithm, followed by manual correction of 80 fascicles, done in an ordinary image editing software. We estimated that pre-annotating using the original algorithm reduced the time of correction by four times compared to manual annotation from scratch.

Fiber Detection

Neurofilament: To detect neurofilament positive pixels, we empirically selected a threshold brightness in the neurofilament color channel (154 out of 256) above which pixels were classified as positive. We further discovered connected components of such pixels to arrive at blobs of neurofilament. Blobs containing less than 10 pixels were excluded as noise. The remaining blobs were broken divided into individual fibers by fitting Gaussian mixture model on them of different number of Gaussian distributions (i.e. number of fibers) and then selecting the best fit determining the amount and location of enclosed axons.

Myelin: Myelin positive pixels were detected using the same technique as described previously [62]. Briefly myelin channel pixels surrounding each detected neurofilament positive axon were analyzed. Pixels were classified as myelin positive when their brightness reached 128 out of 256. First, the outside pixel shell of neurofilament positive fibers were taken and neighboring pixels were recursively checked (for a maximum of 5 recursive steps) for myelin positive pixels. If more than 30% of fiber neighboring pixels were found to be myelin positive, the said fiber was classified as myelinated.

ChAT: Similar to Neurofilament and myelin pixel classification, we empirically selected a brightness threshold, applied to the chat color channel, of 131 out of 256. Chat positive pixels overlapping myelinated axons were counted separately for each fiber and if more than 5% of pixels were found to be chat positive, we regarded the fiber as chat positive.

The final set of segmentations was performed by the combination of the standard computer vision and deep learning algorithms: we let Mask R-CNN detect axons first, then opted for traditional methods to detect and divide overlapping neurafilament blobs that were ignored by the deep learning model. This combination achieved a fiber detection accuracy of 96% [75]

After the instance segmentation of neurafilament and the assignment of myelin to detected fibers, we extracted a set of features for each axon. These features include the longer and shorter diameters, the perimeter, and area of the fiber, in addition to the thickness of the myelin, and the polar coordinates of the fiber relative to the center of mass of the enclosing fascicle.

We manually annotated nerve cross-sections on the fascicle level to derive polar coordinates of fascicles and their distance from the epineurium. Moreover, we extracted fascicle-level features including the perimeter of

the perinerium, the area of the fascicle enclosed by the perinerium, and the total count and area of each fiber type within a fascicle.

Nav1.8: Similar to generate ground truth for the deep learning instance segmentation network, we performed manual annotation of NAV1.8 stained images to determine the density of C fibers within bundles given the area of the enclosing bundle. Due to the low resolution of light microscopy at the range of 1 µm, we used Airyscan equipped super high resolution confocal microscope captured laser microscopy images of parts of fascicles, from which single NAV1.8 positive C fibers can be distinguished (Suppl. Figure S11, a). These high resolution images were manually annotated bundle-by-bundle to amass counts of fibers within more than 300 bundles extracted from two animals and four different fascicles. To predict number of NAV1.8 positive C fibers from lower resolution light microscopy images (Suppl. Figure S11, c) a linear regression model was fit on the C fiber counts given the area of the bundle (R^2 = XY) (Suppl. Figure S11, d). We subsequently employed the linear regression model to estimate the number of NAV1.8 positive C fibers in clouds of NAV1.8 stains, detected as bundles, in light microscopy images (Suppl. Figure S11, e). As the linear regression model estimates are real numbers, we round those numbers to the closest integer for each detected bundle to get actual counts.

All images are preprocessed before the segmentation to enhance contrast and to remove noise. Myelin-neurafilament-chat-stained images were first adjusted by adaptive histogram equalization (dividing each fascicle image into a 32-by-32 grid), then color clipped by defining upper and lower threshold of the clip for separately each cross section manually. The thresholds for each cross-section and channel were selected to remove background noise and to render the stains close to binary (distinct foreground and background), which removed the brightness variance between cross-sections allowing us to use the same parameters for all cross-sections in the subsequent segmentation process. NAV1.8 images were not processed by adaptive histogram equalization, but were color clipped as described above. In the subsequent segmentation process, we ignore all individual neurafilament and NAV1.8 blobs that are smaller than 0.225 um^2, which we found to be background noise rather than actual fibers.

Data analysis

Once we detected and localized fibers and fascicles, and further extracted features from them, we performed subsequent analysis to map the distribution of different fiber types within-fascicle, and within the whole nerve.

We calculated within-fascicle counts and areas of the four fiber types, namely, myelinated efferents (MEff), myelinated afferents (MAff), unmyelinated efferents (UEff) and unmyelinated afferents (UAff). The per-fascicle counts are either presented in their absolute values (Figure 3A, I-L) or as percentages normalized by the total fiber count per fascicle (Figure 3C).

For each fiber type we estimated the ratio of its neighboring fiber types in a 15 µm radius (Figure 3E, c). For each fiber in every fascicle at the mid-cervical level, we captured its neighboring fibers using k-nearest neighbors, then filtered out the ones outside of the 15 µm radius of the fiber. We accumulated the counts of neighboring fiber types for each center fiber type; normalized by the total count of neighbors we calculated the overall ratio of a fibers a given type being in the neighborhood of a given fiber type. To further describe the tendency of different fiber types to share space, we compared their total numbers in each fascicle (Figure 3D, a & b). Within-fascicle mixing was analyzed by splitting each mid-cervical fascicle into a grid of 30-by-30 µm non-overlapping spatial sectors, establish the fiber counts by type in the sectors, then finally count the number of sectors of a certain composition and represent the propensity of two fiber types to share a space of 30-µm-width fascicle area by showing a 2D histogram of the distribution of compositions of the two fiber types (Figure 3E, a & b)

To examine distribution of fiber types within the nerve, we measured the percentage of a fiber type being positioned in fascicles inside rings of 100-µm width at different distances from the epinerium. We show the

overall distribution of fiber types as the function of epinerium distance combining data extracted from nerves of different animals at the mid-cervical level (Suppl. Figure S14, A). We also present the same information for individual nerves as cumulative distributions (Suppl. Figure S15). We grouped fascicles according to their effective diameter into 50 -µm bins and measured the percent area occupied by each fiber type within each fascicle normalized by the area of the fascicle. We then computed the average and standard deviation of such fiber type percentages per effective diameter bin (Suppl. Figure S14, B).

As we manually annotated single fibers of MEff, MAff, UEff and UAff to generate ground truth data for our instance segmentation and NAV1.8 positive C fiber counting model, we had access to accurate single-fiber features. To gauge the size of the different fiber types, we measured the effective diameter of the manually annotated single fibers of each type and presented their distribution (Suppl. Figure S12).

References

1. Settell, M.L., et al., *Functional vagotopy in the cervical vagus nerve of the domestic pig: implications for the study of vagus nerve stimulation.* J Neural Eng, 2020. **17**(2): p. 026022.
2. Stakenborg, N., et al., *Comparison between the cervical and abdominal vagus nerves in mice, pigs, and humans.* Neurogastroenterol Motil, 2020. **32**(9): p. e13889.
3. Pelot, N.A., et al., *Quantified Morphology of the Cervical and Subdiaphragmatic Vagus Nerves of Human, Pig, and Rat.* Front Neurosci, 2020. **14**: p. 601479.
4. Thompson, N., S. Mastitskaya, and D. Holder, *Avoiding off-target effects in electrical stimulation of the cervical vagus nerve: Neuroanatomical tracing techniques to study fascicular anatomy of the vagus nerve.* J Neurosci Methods, 2019. **325**: p. 108325.
5. Kenny, B.J. and B. Bordoni, *Neuroanatomy, Cranial Nerve 10 (Vagus Nerve)*, in *StatPearls*. 2021: Treasure Island (FL).
6. Stewart, J.D., *Peripheral nerve fascicles: anatomy and clinical relevance.* Muscle Nerve, 2003. **28**(5): p. 525-41.
7. De Ferrari, G.M., et al., *Long-term vagal stimulation for heart failure: Eighteen month results from the NEural Cardiac TherApy foR Heart Failure (NECTAR-HF) trial.* Int J Cardiol, 2017. **244**: p. 229-234.
8. Sinniger, V., et al., *A 12-month pilot study outcomes of vagus nerve stimulation in Crohn's disease.* Neurogastroenterol Motil, 2020. **32**(10): p. e13911.
9. Doko, I., et al., *[Vagal Nerve Stimulation in the Treatment of Patients with Rheumatoid Arthritis - Results through Day 84 Obtained at the Croatian Center of an International Pilot Study].* Reumatizam, 2016. **63**(2): p. 1-8.
10. Giordano, F., et al., *Vagus nerve stimulation: Surgical technique of implantation and revision and related morbidity.* Epilepsia, 2017. **58 Suppl 1**: p. 85-90.
11. Nicolai, E.N., et al., *Sources of off-target effects of vagus nerve stimulation using the helical clinical lead in domestic pigs.* J Neural Eng, 2020. **17**(4): p. 046017.
12. Hoffman, H.H. and H.N. Schnitzlein, *The numbers of nerve fibers in the vagus nerve of man.* Anat Rec, 1961. **139**: p. 429-35.
13. Pelot, N.A. and W.M. Grill, *Effects of vagal neuromodulation on feeding behavior.* Brain Res, 2018. **1693**(Pt B): p. 180-187.
14. Musselman, E.D., N.A. Pelot, and W.M. Grill, *Empirically Based Guidelines for Selecting Vagus Nerve Stimulation Parameters in Epilepsy and Heart Failure.* Cold Spring Harb Perspect Med, 2019. **9**(7).
15. Fitchett, A., S. Mastitskaya, and K. Aristovich, *Selective Neuromodulation of the Vagus Nerve.* Front Neurosci, 2021. **15**: p. 685872.
16. Aristovich, K., et al., *Model-based geometrical optimisation and in vivo validation of a spatially selective multielectrode cuff array for vagus nerve neuromodulation.* J Neurosci Methods, 2021. **352**: p. 109079.
17. Erman, A.B., et al., *Disorders of cranial nerves IX and X.* Semin Neurol, 2009. **29**(1): p. 85-92.
18. Yuan, H. and S.D. Silberstein, *Vagus Nerve and Vagus Nerve Stimulation, a Comprehensive Review: Part I.* Headache, 2016. **56**(1): p. 71-8.
19. Weijs, T.J., et al., *Topography and extent of pulmonary vagus nerve supply with respect to transthoracic oesophagectomy.* J Anat, 2015. **227**(4): p. 431-9.
20. Yang, M., X. Zhao, and R.R. Miselis, *The origin of catecholaminergic nerve fibers in the subdiaphragmatic vagus nerve of rat.* J Auton Nerv Syst, 1999. **76**(2-3): p. 108-17.
21. Muryobayashi, T., et al., *Fluorescence histochemical demonstration of adrenergic nerve fibers in the vagus nerve of cats and dogs.* Jpn J Pharmacol, 1968. **18**(3): p. 285-93.
22. Onkka, P., et al., *Sympathetic nerve fibers and ganglia in canine cervical vagus nerves: localization and quantitation.* Heart Rhythm, 2013. **10**(4): p. 585-91.
23. Lundberg, J., et al., *Catecholamine-containing nerve fibres in the human abdominal vagus.* Gastroenterology, 1976. **70**(3): p. 472-4.
24. Djouhri, L. and S.N. Lawson, *Abeta-fiber nociceptive primary afferent neurons: a review of incidence and properties in relation to other afferent A-fiber neurons in mammals.* Brain Res Brain Res Rev, 2004. **46**(2): p. 131-45.
25. Mazzone, S.B. and B.J. Undem, *Vagal Afferent Innervation of the Airways in Health and Disease.* Physiol Rev, 2016. **96**(3): p. 975-1024.
26. Canning, B.J. and B.J. Undem, *Evidence that distinct neural pathways mediate parasympathetic contractions and relaxations of guinea-pig trachealis.* J Physiol, 1993. **471**: p. 25-40.
27. Reese, S. and C. Ruppert, *Ultrasonographic imaging of the vagosympathetic trunk in the dog.* Vet Radiol Ultrasound, 2001. **42**(3): p. 272-5.
28. Lee, L.Y. and T. Horikawa, *Development of alternating, ipsilateral Horner syndrome and Pourfour du Petit syndrome associated with oesophagostomy tube placement in a cat.* JFMS Open Rep, 2021. **7**(1): p. 2055116920984379.

29. Verlinden, T.J., et al., *Morphology of the human cervical vagus nerve: implications for vagus nerve stimulation treatment.* Acta Neurol Scand, 2016. **133**(3): p. 173-82.
30. Kawagishi, K., et al., *Tyrosine hydroxylase-immunoreactive fibers in the human vagus nerve.* J Clin Neurosci, 2008. **15**(9): p. 1023-6.
31. Belvisi, M.G., *Sensory nerves and airway inflammation: role of A delta and C-fibres.* Pulm Pharmacol Ther, 2003. **16**(1): p. 1-7.
32. Pavlov, V.A., S.S. Chavan, and K.J. Tracey, *Molecular and Functional Neuroscience in Immunity.* Annu Rev Immunol, 2018. **36**: p. 783-812.
33. Chang, R.B., et al., *Vagal Sensory Neuron Subtypes that Differentially Control Breathing.* Cell, 2015. **161**(3): p. 622-633.
34. Chen, S.L., et al., *Subdiaphragmatic vagal afferent nerves modulate visceral pain.* Am J Physiol Gastrointest Liver Physiol, 2008. **294**(6): p. G1441-9.
35. Seki, A., et al., *Sympathetic nerve fibers in human cervical and thoracic vagus nerves.* Heart Rhythm, 2014. **11**(8): p. 1411-7.
36. Cai, Q.Q., et al., *Distribution of dopamine receptors D1- and D2-immunoreactive neurons in the dorsal motor nucleus of vagus in rats.* Auton Neurosci, 2013. **176**(1-2): p. 48-53.
37. Moffatt, J.D., B. Dumsday, and J.R. McLean, *Characterization of non-adrenergic, non-cholinergic inhibitory responses of the isolated guinea-pig trachea: differences between pre- and post-ganglionic nerve stimulation.* Br J Pharmacol, 1999. **128**(2): p. 458-64.
38. Asala, S.A. and A.J. Bower, *An electron microscope study of vagus nerve composition in the ferret.* Anat Embryol (Berl), 1986. **175**(2): p. 247-53.
39. Kim, S.H., et al., *Mapping of Sensory Nerve Subsets within the Vagal Ganglia and the Brainstem Using Reporter Mice for Pirt, TRPV1, 5-HT3, and Tac1 Expression.* eNeuro, 2020. **7**(2).
40. Mata, M., D. Alessi, and D.J. Fink, *S100 is preferentially distributed in myelin-forming Schwann cells.* J Neurocytol, 1990. **19**(3): p. 432-42.
41. Harty, B.L. and K.R. Monk, *Unwrapping the unappreciated: recent progress in Remak Schwann cell biology.* Curr Opin Neurobiol, 2017. **47**: p. 131-137.
42. Grill, W.M., S.E. Norman, and R.V. Bellamkonda, *Implanted neural interfaces: biochallenges and engineered solutions.* Annu Rev Biomed Eng, 2009. **11**: p. 1-24.
43. Lotti, F., et al., *Invasive Intraneural Interfaces: Foreign Body Reaction Issues.* Front Neurosci, 2017. **11**: p. 497.
44. Ahmed, U., et al., *Implant- and anesthesia-related factors affecting cardiopulmonary threshold intensities for vagus nerve stimulation.* J Neural Eng, 2021. **18**(4).
45. Peclin, P. and J. Rozman, *Alternative paradigm of selective vagus nerve stimulation tested on an isolated porcine vagus nerve.* ScientificWorldJournal, 2014. **2014**: p. 310283.
46. Settell, M.L., et al., *In vivo Visualization of Pig Vagus Nerve "Vagotopy" Using Ultrasound.* Front Neurosci, 2021. **15**: p. 676680.
47. Hammer, N., et al., *Human vagus nerve branching in the cervical region.* PLoS One, 2015. **10**(2): p. e0118006.
48. Havton, L.A., et al., *Human organ donor-derived vagus nerve biopsies allow for well-preserved ultrastructure and high-resolution mapping of myelinated and unmyelinated fibers.* Sci Rep, 2021. **11**(1): p. 23831.
49. Katz, D.M. and H.J. Karten, *Subnuclear organization of the dorsal motor nucleus of the vagus nerve in the pigeon, Columbia livia.* J Comp Neurol, 1983. **217**(1): p. 31-46.
50. Katz, D.M. and H.J. Karten, *Topographic representation of visceral target organs within the dorsal motor nucleus of the vagus nerve of the pigeon Columba livia.* J Comp Neurol, 1985. **242**(3): p. 397-414.
51. Huang, X.F., I. Tork, and G. Paxinos, *Dorsal motor nucleus of the vagus nerve: a cyto- and chemoarchitectonic study in the human.* J Comp Neurol, 1993. **330**(2): p. 158-82.
52. Broussard, D.L. and S.M. Altschuler, *Brainstem viscerotopic organization of afferents and efferents involved in the control of swallowing.* Am J Med, 2000. **108 Suppl 4a**: p. 79S-86S.
53. Agostoni, E., et al., *Functional and histological studies of the vagus nerve and its branches to the heart, lungs and abdominal viscera in the cat.* J Physiol, 1957. **135**(1): p. 182-205.
54. Chang, Y.C., et al., *Quantitative estimation of nerve fiber engagement by vagus nerve stimulation using physiological markers.* Brain Stimul, 2020. **13**(6): p. 1617-1630.
55. Mei, N., M. Condamin, and A. Boyer, *The composition of the vagus nerve of the cat.* Cell Tissue Res, 1980. **209**(3): p. 423-31.
56. Schemann, M., et al., *Identification of cholinergic neurons in enteric nervous system by antibodies against choline acetyltransferase.* Am J Physiol, 1993. **265**(5 Pt 1): p. G1005-9.
57. Kressel, M. and M. Radespiel-Troger, *Anterograde tracing and immunohistochemical characterization of potentially mechanosensitive vagal afferents in the esophagus.* J Comp Neurol, 1999. **412**(1): p. 161-72.
58. Veraart, C., W.M. Grill, and J.T. Mortimer, *Selective control of muscle activation with a multipolar nerve cuff electrode.* IEEE Trans Biomed Eng, 1993. **40**(7): p. 640-53.

59. Gierthmuehlen, M., et al., *Haemodynamic Responses to Selective Vagal Nerve Stimulation under Enalapril Medication in Rats.* PLoS One, 2016. **11**(1): p. e0147045.
60. Ravagli, E., et al., *Fascicle localisation within peripheral nerves through evoked activity recordings: A comparison between electrical impedance tomography and multi-electrode arrays.* J Neurosci Methods, 2021. **358**: p. 109140.
61. Zaqout, S., L.L. Becker, and A.M. Kaindl, *Immunofluorescence Staining of Paraffin Sections Step by Step.* Front Neuroanat, 2020. **14**: p. 582218.
62. Toth, V., et al., *Single-axon level automatic segmentation and feature extraction from immuhistochemical images of peripheral nerves.* Annu Int Conf IEEE Eng Med Biol Soc, 2020. **2020**: p. 1859-1862.
63. Yuxin Wu, A.K., Francisco Massa, Wan-Yen Lo and and Ross Girshick. , *Detectron2.* 2019.
64. Viktor Tóth, N.J., Adam Abbas, Moontahinaz Rob, Ariba Khan, Stavros Zanos, Theodoros P. Zanos *Single-axon level segmentation and feature extraction pipeline combining traditional and deep learning computer vision algorithms.* Abstracts from the Fourth Bioelectronic Medicine Summit:, 2020: p. P16. .